Article

Effects of Radiation Damage on Metal-Binding Sites in Thermolysin

Ki Hyun Nam

College of General Education, Kookmin University, Seoul 02707, Republic of Korea; structure@kookmin.ac.kr

Abstract: Radiation damage is an inherent problem in macromolecular crystallography because it impairs the diffraction quality of crystals and produces inaccurate structural information. Understanding radiation damage in protein structures is crucial for accurate structural interpretation and effective data collection. This study undertook X-ray data collection and structure determination of thermolysin (TLN), which contains Zn and Ca ions, by using three different X-ray doses to improve our understanding of the radiation damage phenomena on metal ions in proteins. Data processing revealed typical global radiation damage in TLN, such as an increase in unit cell volume, R_{merge} value, and Wilson B-factor. An analysis of the B-factor indicated that radiation damage at the Zn and Ca sites in TLN increased with higher X-ray doses. However, the distance between the metal ions and their interacting residues in TLN was not significantly affected, suggesting that radiation damage to the metal ions has a minimal effect on these interactions. Moreover, the increase in the B-factor of the metal ions according to the X-ray dose was similar to that in the B-factor of the residues interacting with the metal ions. These results expand our understanding of radiation damage phenomena in macromolecules and can be used to improve data collection strategies.

Keywords: radiation damage; thermolysin; metal ion; B-factor; electron density map

1. Introduction

Macromolecular crystallography provides valuable information for understanding the structure and function of biological macromolecules [1,2]. This structural information offers insights for developing new drugs and engineering proteins to improve industrial enzymes [3–7]. Providing accurate structural information at high resolution is crucial for understanding the exact molecular mechanisms and for designing successful applied research [8–10]. Collecting high-resolution data involves many factors, including crystal quality, X-ray properties, detector specifications, and data processing programs. Among these factors, providing intense X-rays with a high photon density to the crystal sample is important in increasing the diffraction intensity of the crystal.

The achievable beam size from low-emission third- and fourth-generation light sources has been reduced [11–13]. The development of optical devices such as Kirkpatrick–Baez mirrors enables the focusing of X-rays at sizes from a few microns to nanometers [14,15]. This microfocused beam not only increases the diffraction intensity of the crystal sample by providing a high density of photons, but also shortens the data collection time, thereby increasing the efficiency of the macromolecular crystallography process [16]. However, despite these advantages, intense X-rays cause significant global and specific radiation damage to crystal samples, resulting in degradation of data quality, structural errors, and even crystal destruction [17–20]. During the process of global radiation damage, free radicals break or modify amino acid bonds [21,22]. This process changes the conformation of amino acids and increases the nonisomorphism of the crystal [21,22]. This disruption of the crystal packing reduces the diffraction intensity of the crystal, leading to the collection of low-resolution data. Typically, global radiation damage is indicated by an increase in unit cell volume, Wilson B-factor, or R_{merge} value [21,22]. Specific radiation damage causes

incorrect structural information at specific atoms or amino acids, such as by breaking or elongating disulfide bonds, decarboxylating side chains of aspartic and glutamic acids, photoreducing metal centers, disorganizing sulfur atoms in methionine, and increasing the B-factor of selenium atoms in selenomethionine [21–28].

Therefore, crystal structures that sustain radiation damage may provide biologically irrelevant or inaccurate structural information [29–31]. This could potentially produce incorrect structural information for subsequent research, such as in drug design or protein engineering for industrial and medical applications. Various experimental and theoretical studies have been conducted to understand the effects and phenomena of radiation damage [18,26,32]. The radiation damage phenomenon that occurs in macromolecular crystallography varies depending not only on the crystal sample, but also on the X-rays used in the experiment, the experimental environment, and the data collection method. Accordingly, conducting radiation damage research based on various data collection scenarios contributes to establishing a data collection strategy that minimizes radiation damage.

Various proteins contain metal ions, which are commonly involved in enzymatic reactions, protein stability, and transport [33–36]. In general, high-Z atoms, such as metal ions, are known to be more sensitive to radiation damage than atoms (C, N, and O) that constitute amino acids [28,37]. Several studies have investigated radiation damage to metal ions in proteins, including the Mn_4Ca complex in photosystem II [38], heme in peroxidase [39], and nickel-containing superoxide dismutase [40]. These studies offer valuable insights into the effects of radiation damage on metal coordination. However, the phenomenon of radiation damage to metal ions contained in proteins is still insufficiently explored in terms of structural analysis.

To extend our knowledge of radiation damage, we investigated radiation damage to the crystal structure of thermolysin (TLN), which contains Zn and Ca ions. X-ray diffraction experiments were performed with large TLN crystals and a microfocusing X-ray beam using a single-point data collection method. Three diffraction datasets of TLN crystals were collected based on three different X-ray doses, and crystal structures were determined at a 1.40 Å resolution. The global and specific radiation damage to TLN, depending on the X-ray dose, was analyzed. Furthermore, the specific radiation damage to metal ions and their interacting residues in TLN was examined. These results provide an improved understanding of the radiation damage phenomenon.

2. Materials and Methods

2.1. Sample Preparation

TLN from *Bacillus thermoproteolyticus* (Cat No. HR7-098, Hampton Research, Aliso Viejo, CA, USA) was dissolved in 50 mM NaOH. The TLN solution was diluted in 10 mM Tris-HCl (pH 8.0) and 200 mM NaCl and then concentrated to 20 mg/mL using a Centricon (MWCO, 10 kDa, Millipore, Burlington, MA, USA) for crystallization. Crystallization was performed using the hanging-drop vapor diffusion method at 22 °C. The TLN solution (2 μL) was mixed with a crystallization solution (2 μL) containing 0.1 M Tris-HCl (pH 8.5), 10% (*v/v*) glycerol, and 1.5 M ammonium sulfate, and equilibrated with 0.5 mL of a reservoir solution. Suitable crystals for X-ray diffraction were obtained within a week. The dimensions of the rod-shaped TLN crystals were approximately $150 \times 150 \times 400$ μm^3.

2.2. X-ray Diffraction and Data Processing

X-ray diffraction data were collected at Beamline 11C at Pohang Light Source II (PLS-II, Pohang, Republic of Korea) [16]. The X-ray wavelength and photon flux were 0.9794 Å and ~5×10^{11} photons/sec, respectively. The X-ray beam size was approximately 3.5×8.5 μm (vertical × horizontal, full width at half maximum) at the sample position. TLN crystals were cryoprotected using a crystallization solution supplemented with 20% (*v/v*) glycerol for 5 s and then mounted on a goniometer under a 100 K liquid nitrogen stream. X-ray diffraction data were collected using a Pilatus 6M detector (Dectris, Baden-Daettwil, Switzerland). Diffraction data were collected by exposing X-rays to three fresh regions of a single rod-shaped crystal for

each of the three exposure times. The X-ray exposure times for the TLN crystal were 100 ms, 500 ms, and 1 s per 1° oscillation, and the total collected oscillation was 360° per dataset. The absorbed X-ray doses were calculated with RADDOSE-3D [41]. The diffraction images were indexed, integrated, and processed using the HKL2000 program [42].

2.3. Structure Determination

The phase problem was solved by the molecular replacement method using MOL-REP [43] from the CCP4 program suite [44]. The crystal structure of thermolysin (PDB: 6LZN) [45] was used as the search model. Manual model building was performed with COOT [46]. Structure refinement was performed with REFMAC5 [47]. Water molecules were automatically added to the model with default parameters during structure refinement. The final coordinates were validated by MolProbity [48]. The coordination of metal ions in TLN structures was validated using CheckMyMetal [49]. The structure figures were generated with PyMOL (http://www.pymol.org, accessed on 8 March 2024).

3. Results

3.1. Data Collection

To improve our understanding of radiation damage to metal ions in proteins, the X-ray diffraction data of TLN were collected using a single-point data collection method. The TLN crystal ($150 \times 150 \times 400$ μm³) used was larger than the X-ray beam size (3.5×8.5 μm, FWHM). Accordingly, the center of the crystal aligned with the X-ray beam was continuously exposed to X-rays during rotation for data collection. This caused accumulated radiation damage in the central region of the crystal. Since X-rays penetrate the crystal sample and the crystal volume was larger than the X-ray size, the unexposed crystal volume was continuously exposed during 180° rotation, and data collected after 180° received accumulated X-ray exposure. The TLN crystals were exposed to X-rays for 100 ms, 500 ms, and 1 s per 1° to investigate X-ray dose-dependent radiation damage, and diffraction data were collected for 360° oscillation. The calculated average diffraction-weighted dose/average doses (exposed region) for TLN^{100ms}, TLN^{500ms}, and TLN^{1s} were approximately 13.01/7.39, 65.06/36.99, and 130.13/73.98 MGy, respectively. The criteria for the resolution cutoff of data for the TLN dataset were set at 100% completeness, >1.6 I/sigma (highest shell), and >0.7 CC1/2 (highest shell). TLN^{100ms}, TLN^{500ms}, and TLN^{1s} were processed to 1.30, 1.35, and 1.30 Å resolutions, respectively (Table 1).

Table 1. Data collection statistics.

Data Collection	TLN^{100ms}	TLN^{500ms}	TLN^{1s}
Beamline	Beamline 11C, PLS-II	Beamline 11C, PLS-II	Beamline 11C, PLS-II
Temperature (K)	100	100	100
Exposure time (ms/°)	100	500	1000
Space group	$P6_122$	$P6_122$	$P6_122$
Unit cell dimension			
a, b, c (Å)	92.919, 92.919, 128.378	93.081, 93.081, 128.694	93.141, 93.141,128.777
α, β, γ (°)	90.00, 90.00, 120.00	90.00, 90.00, 120.00	90.00, 90.00, 120.00
Resolution range (Å)	50.0–1.35 (1.37–1.35)	50.0–1.30 (1.32–1.30)	50.0–1.35 (1.37–1.35)
No. of unique reflections	72,111 (3536)	81,578 (3991)	74,793 (3665)
Completeness (%)	100.0 (100.0)	100.0 (100.0)	100.0 (100.0)
Redundancy	38.4 (33.3)	35.7 (22.5)	32.6 (14.0)
I/sigma(I)	28.25 (2.00)	31.94 (1.76)	32.89 (1.60)
R_{merge}	0.144 (0.422)	0.169 (0.472)	0.317 (3.771)
R_{meas}	0.146 (1.617)	0.172 (2.406)	0.322 (3.907)
CC1/2	0.998 (0.859)	0.998 (0.762)	0.996 (0.703)

Values for the outer shell are given in parentheses.

All TLN crystals belonged to the hexagonal space group $P6_122$. The lengths of the a and b axes of TLN^{100ms}, TLN^{500ms}, and TLN^{1s} determined via unit cell analysis were 92.91, 93.08, and 93.14 Å, respectively, while the lengths of the c axis were 128.378, 128.694, and 128.777 Å. This indicated that the unit cell volume increased with X-ray exposure time, showing typical evidence of global radiation damage. Data processing showed that the overall I/sigma(I) values of TLN^{100ms}, TLN^{500ms}, and TLN^{1s} were 28.25, 31.94, and 32.89, respectively. This indicated an increase in the overall I/sigma value with longer X-ray exposure, especially at a low resolution with X-ray exposure (Figure 1A). In theory, global radiation damage should reduce the diffraction intensity of Bragg peaks with increasing exposure time of microfocused X-rays on the crystal sample; however, the I/sigma increases with extended X-ray exposure time because the crystal is larger than the X-ray beam. The quality of the statistical values of R_{merge}, R_{meas}, and CC1/2 significantly decreased with the increased amount of X-ray exposure (Figure 1B–D). The overall R_{merge}/R_{meas} values of TLN^{100ms}, TLN^{500ms}, and TLN^{1s} were 0.144/0.146, 0.169/0.172, and 0.317/0.322, respectively, indicating that the R_{merge} and R_{meas} values increased in proportion to the X-ray exposure time. No significant difference occurred in R_{merge}/R_{meas} between data up to 50–3 Å, whereas at < 3 Å, the R-values significantly increased because of X-ray exposure (Figure 1B,C). No significant difference was present in CC1/2 values for the TLN data within the 50–3 Å range based on X-ray dose. However, at resolutions < 2 Å, a decrease in CC1/2 values was observed with increasing X-ray dose (Figure 1D).
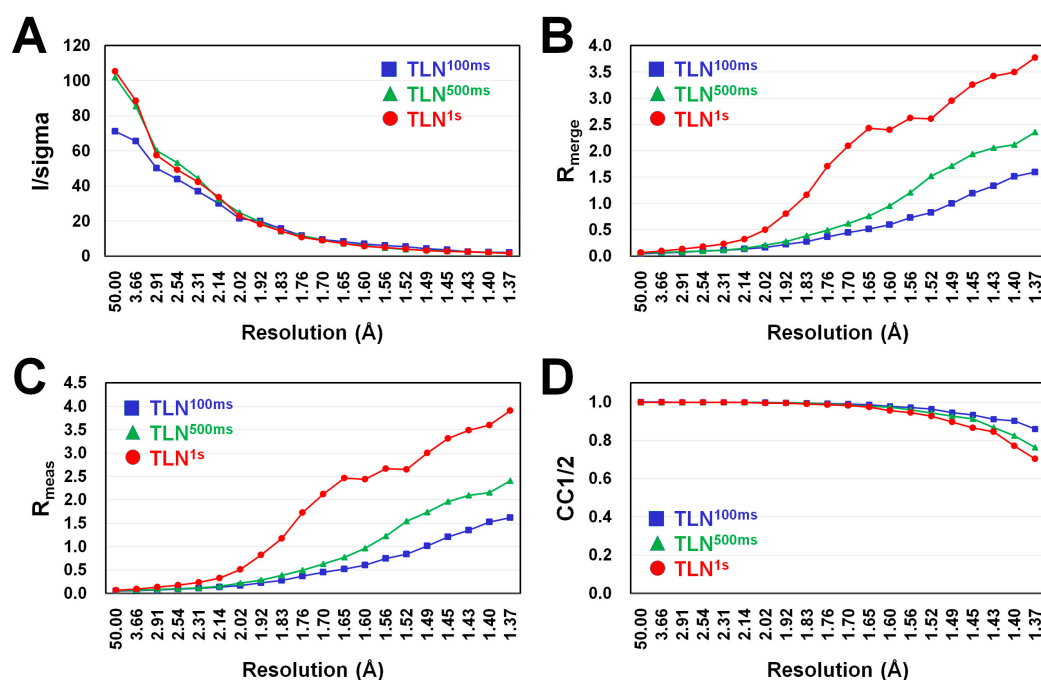

Figure 1. Analysis of data collection statistics of TLN dataset depending on X-ray exposure time. (**A**) I/sigma, (**B**) R_{merge}, (**C**) R_{meas}, and (**D**) CC1/2 values of TLN^{100ms}, TLN^{500ms}, and TLN^{1s}.

3.2. Structure Analysis

The crystal structures of TLN were determined to understand the radiation damage to the overall structure and metal-binding sites depending on the X-ray dose. The refinement statistics and quality of electron density maps, as well as temperature factor values, varied depending on the data resolution. Accordingly, the refinement resolution range of all TLN datasets was unified to 35–1.40 Å (Table 2). The electron density map of all TLN samples was clear enough to build the entire sequence from Ile1 to Lys316. All water molecules were automatically added to the TLN structures during structure refinement with default parameters to avoid bias. TLN^{100ms}, TLN^{500ms}, and TLN^{1s} contained 404, 371, and 344 defined water molecules, respectively. The R_{work}/R_{free} values of the TLN^{100ms}, TLN^{500ms},

and TLN^{1s} structures were 14.82/16.73, 14.94/16.84, and 15.18/14.22, respectively. This indicated that the R-values tended to increase as the X-ray dose increased. The B-factors of TLN^{100ms}, TLN^{500ms}, and TLN^{1s} were 11.64, 12.00, and 13.06 Å^2, respectively, while those of the water molecules for TLN^{100ms}, TLN^{500ms}, and TLN^{1s} were 26.29, 26.68, and 27.51 Å^2, respectively. This indicates that the quality of the electron density maps corresponding to amino acid and water molecules deteriorated as the X-ray dose increased.

Table 2. Structure refinement statistics.

Refinement	TLN^{100ms}	TLN^{500ms}	TLN^{1s}
Resolution range (Å)	34.09–1.40	34.16–1.40	34.18–1.40
R_{work}[a]	0.14822	0.14948	0.15182
R_{free}[b]	0.16730	0.16843	0.17244
R.m.s. deviations			
Bonds (Å)	0.012	0.012	0.012
Angles (°)	1.780	1.801	1.758
Average B factors (Å^2)			
Protein	11.642	12.001	13.603
Water	26.294	26.688	27.514
Ramachandran plot			
Most favored (%)	96.2	96.2	96.5
Allowed (%)	3.8	3.8	3.5
PDB code	8ZM4	8ZM5	8ZM6

[a] $R_{work} = \Sigma ||F_{obs}| \Sigma |F_{calc}||/\Sigma |F_{obs}|$, where Fobs and F$_{calc}$ are the observed and calculated structure factor amplitudes, respectively. [b] R$_{free}$ was calculated as R$_{work}$ using a randomly selected subset of unique reflections not used for structural refinement.

TLN comprises two approximately globular N- and C-terminal domains with a gap spanning the center of the molecule (Figure 2A). A Zn ion, which is involved in protease activity, is located in the central α-helix between the two domains, and four Ca ions involved in protein stability and enzyme activity are located in the outer loop regions (Figure 2A). Superimposition of TLN^{100ms}, TLN^{500ms}, and TLN^{1s} showed structural similarity, with root mean square deviation of 0.02–0.05 Å, indicating no significant radiation damage to the main chain of the TLN structure. The B-factor is used to evaluate protein radiation damage. The B-factor putty representation showed that the B-factors of the loop regions of TLN slightly increased with the increasing X-ray dose (Figure 2B–D). B-factor plot analysis revealed that TLN^{100ms} and TLN^{500ms} were similar, whereas TLN1s had a relatively high B-factor value (Figure 2E). The normalized B-factor analysis showed no significant change in the B-factor for any specific region (Figure 2E). These results indicate that the TLN B-factor value increases with increasing X-ray exposure but without a particular tendency for that of specific amino acid regions to increase further.
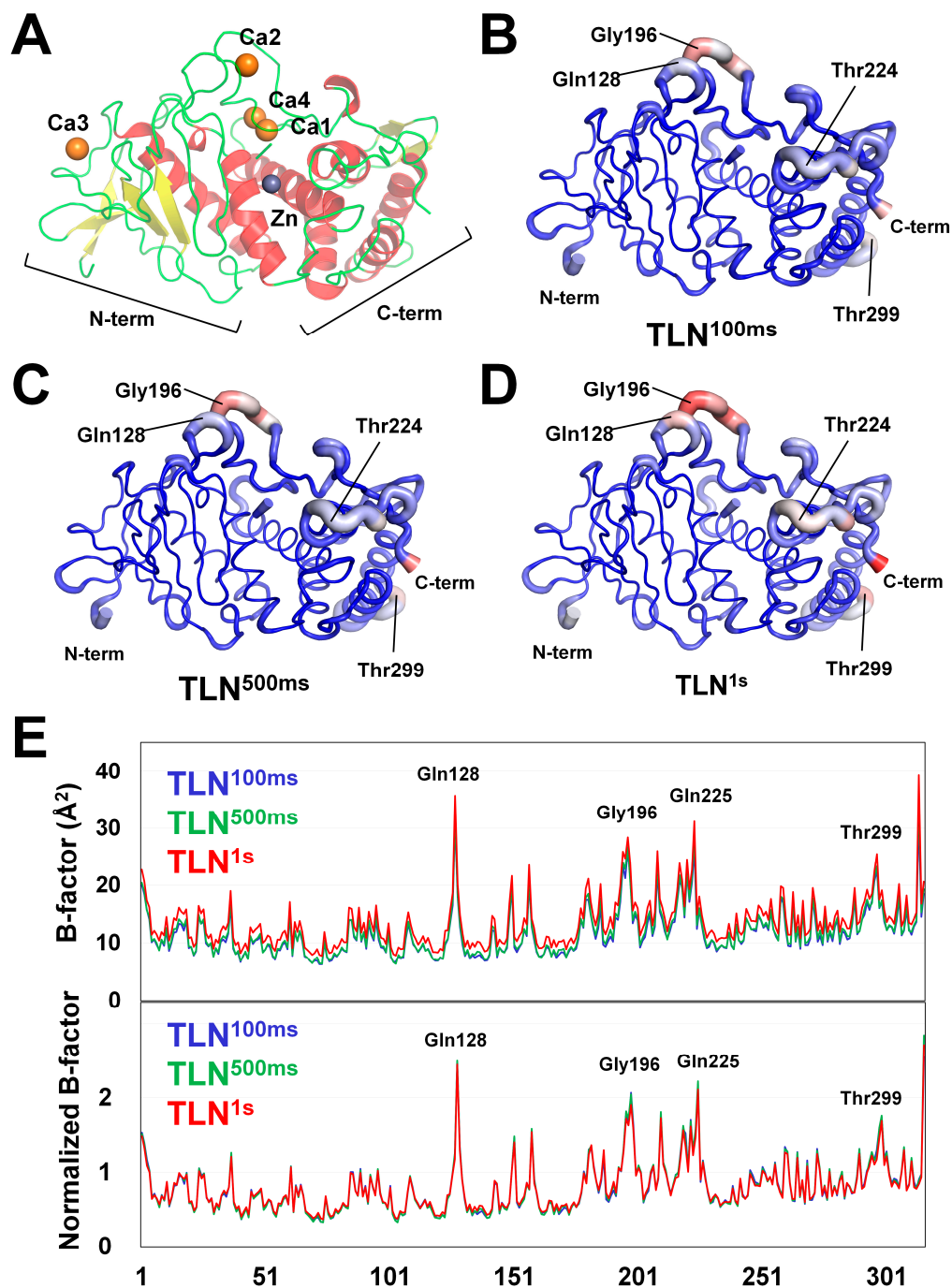
Figure 2. Analysis of temperature factor of TLN dependent on X-ray dose. (**A**) Crystal structure of TLN. B-factor putty representation of (**B**) TLN^{100ms}, (**C**) TLN^{500ms}, and (**D**) TLN^{1s}. (**E**) Profile of B-factors and normalized B-factor of TLN^{100ms}, TLN^{500ms}, and TLN^{1s}.

3.3. Metal Ion–Binding Sites

High-Z atoms, such as metal ions, are sensitive to radiation damage [28,37]. TLN contains a Zn ion, which is involved in hydrolase activity, and four Ca ions, which contribute to thermal stability [50]. To verify metal ion-binding to the TLN molecule, the initial structure refinement of TLN datasets was performed without metal ions. The results showed strong positive Fo–Fc electron density maps (>10 sigma) corresponding to one Zn and four Ca ions at previously described metal-binding sites in TLN (Supplementary Figure S1). Further structure refinement of TLNs with Zn and Ca ions was performed. The validation of metal ion coordination in TLNs, including geometry and gRMSD, is presented

in Table S1. The refinement revealed partial negative Fo–Fc electron density maps for Zn and Ca1, indicating low occupancy. The volume of the negative Fo–Fc electron density map for Zn and Ca sites did not show a particular tendency to increase with increasing X-ray exposure time (Figure 3). The B-factors of the Zn ion in TLN[100ms], TLN[500ms], and TLN[1s] were 13.24, 13.47, and 15.23 Å^2, respectively, while those of Ca1/Ca2/Ca3/Ca4 in TLN[100ms], TLN[500ms], and TLN[1s] were 8.61/12.91/8.46/18.16, 9.20/13.37/9.01/19.64, and 10.86/14.97/10.66/21.91 Å^2, respectively. These results indicate that the B-factor increased with increasing X-ray exposure time. Meanwhile, positive Fo–Fc electron density maps were observed near the Zn-binding site (Supplementary Figure S2), which have also been observed in previous serial crystallography studies [51] but were not identified. Since it was unclear what this density corresponded to, no molecule was added to the final model, and the description is excluded here.
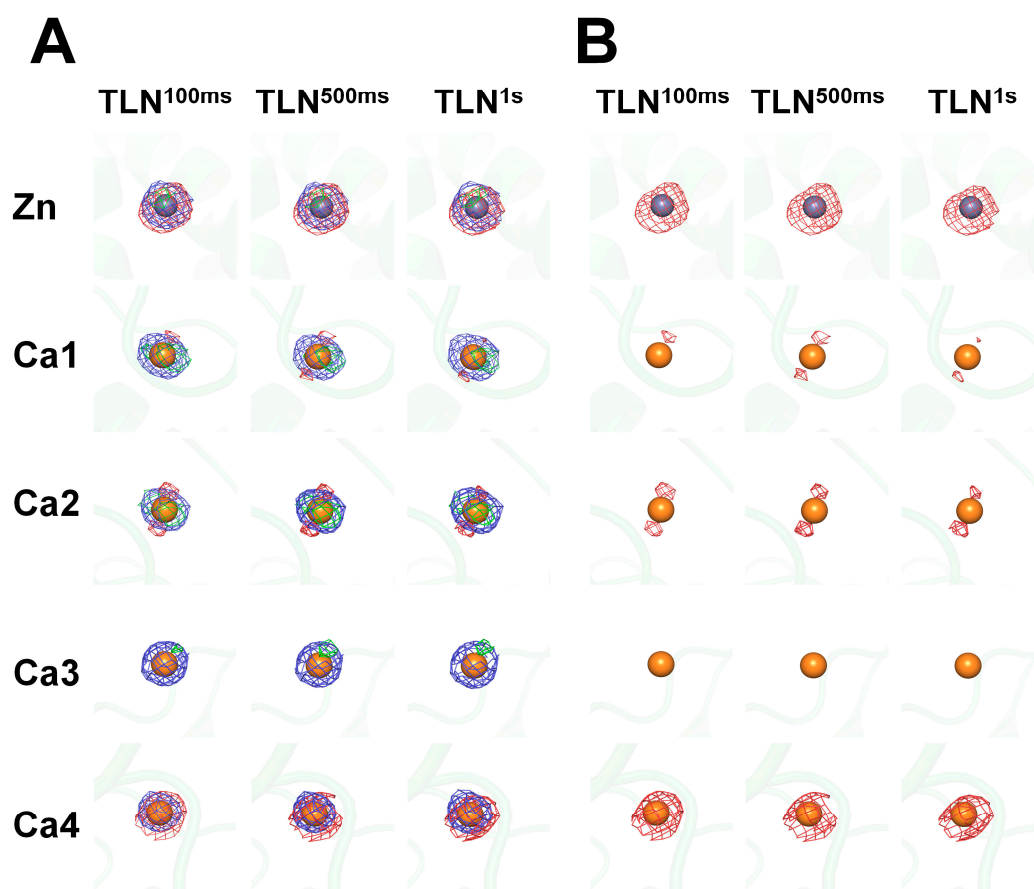

Figure 3. Analysis of electron density maps for metal-binding sites of TLNs. (**A**) 2Fo–Fc (blue mesh, 5σ) and Fo–Fc (green mesh, 3σ) omit maps for Zn- and Ca-binding sites of TLN[100ms], TLN[500ms], and TLN[1s]. (**B**) 2Fo–Fc (blue mesh, 5σ) and Fo–Fc (green mesh, 3σ; red mesh, −3σ) electron density maps for Zn- and Ca-binding sites of TLN[100ms], TLN[500ms], and TLN[1s] after refinement with metal ions.

The distances between the metal ions and their interacting residues were measured to understand whether the increase in the B-factors of the metal-binding sites affected the interaction between the metal ions and TLN (Table 3).

The Zn-binding site was coordinated by His142 (distance range between TLN[100ms], TLN[500ms], and TLN[1s]: 2.09–2.10 Å), His146 (2.03–2.05 Å), and Glu166 (2.08–2.11 Å) (Figure 4A). The Ca1-binding site was coordinated by Asp138 (2.38–2.40 Å), Glu177 (2.53–2.54 Å /2.58–2.60 Å for OE1/OE2), Asp185 (2.42–2.45 Å), Glu187 (2.36–2.38 Å), and Glu190 (2.56–2.58 /2.45–2.47 Å for OE1/OE2) (Figure 4B). The Ca2-binding site was coordinated by Tyr193 (2.33 Å), Thr194 (2.43–2.44 Å), Thr194 (2.40–2.42 Å), Ile197 (2.24–2.27 Å), and Asp200 (2.34–2.37 Å) (Figure 4C). The Ca3-binding site was coordinated by Asp57 (2.57 Å), Asp57 (2.38 Å), Asp59

(2.38–2.39 Å), and Gln61 (2.28–2.30 Å) (Figure 4D). The Ca4-binding site was coordinated by Glu177 (2.75–2.79 Å), Asn183 (2.27–2.29 Å), Asp185 (2.39–2.40 Å), and Glu190 (2.34–2.37 Å) (Figure 4E). The superimposition of the Zn and Ca ion-binding sites of TLN^{100ms}, TLN^{500ms}, and ^{TLN1s} showed almost identical positioning and conformation of metal-interacting residues (Figure 4). Consequently, B-factors at the metal ion site increased with the X-ray dose, but no significant trends or changes were observed in the distances between the amino acids interacting with these metal ions.

Table 3. Distance between metal ions and metal ion-interacting residues of TLN.

Metal Ion	Residues (atom)	TLN^{100ms}	TLN^{500ms}	TLN^{1s}
Zn	His142 (NE2)	2.10	2.09	2.09
	His146 (NE2)	2.03	2.03	2.05
	Glu166 (OE2)	2.08	2.10	2.11
Ca1	Asp138 (OD2)	2.40	2.38	2.38
	Glu177 (OE1/OE2)	2.53/2.58	2.53/2.60	2.54/2.59
	Asp185 (OD1)	2.42	2.45	2.45
	Glu187 (O)	2.38	2.36	2.36
	Glu190 (OE1/OE2)	2.56/2.45	2.57/2.47	2.58/2.45
Ca2	Tyr193 (O)	2.33	2.33	2.33
	Thr194 (O/OG1)	2.40/2.44	2.42/2.43	2.42/2.44
	Ile197 (O)	2.24	2.24	2.27
	Asp200 (OD1)	2.34	2.37	2.35
Ca3	Asp57 (OD1/OD2)	2.57/2.38	2.57/2.38	2.57/2.38
	Asp59 (OD1)	2.39	2.38	2.39
	Gln61 (O)	2.30	2.28	2.28
Ca4	Glu177 (OE2)	2.75	2.77	2.79
	Asn183 (O)	2.28	2.29	2.27
	Asp185 (OD2)	2.39	2.39	2.40
	Glu190 (OE2)	2.34	2.35	2.37

Next, the B-factors of the metal-binding amino acids were investigated according to the X-ray dose. All metal-binding residues showed a tendency for B-factors to increase as the X-ray dose increased. Compared with the overall B-factor and normalized B-factor of TLN^{100ms}, those of TLN^{500ms} and TLN^{1s} increased by approximately < 10.8% and 15%–30%, respectively. Next, when the X-ray exposure time was increased to TLN^{100ms} and TLN^{1s}, the changes in the B-factors of the metal ions and metal-interacting residues were compared. At the Zn site, the B-factor of the Zn ion was larger than that of the interacting residues (Figure 5A). The B-factors (normalized B-factor values in TLN^{1s}/TLN^{100ms}) of the Zn ion and the interacting residues were 2.0 Å^2 (1.15) and 1.4–2.0 Å^2 (1.15–1.22), respectively. At the Ca1 site, the B-factor of the Asp185, Glu187, and Glu190 residues was larger than that of the Zn ion (Figure 5B) at 2.3 Å^2 (1.27) and 1.9–4.1 Å^2 (1.21–1.28), respectively. At the Ca2 site, the B-factor of the Ca2 ion was smaller than that of the interacting residues (Figure 5C) at 2.1 Å^2 (1.16) and 2.2–3.5 Å^2 (1.16–1.18), respectively. At the Ca3 site, the B-factor of the Ca3 ion was smaller than that of the interacting residues (Figure 5D) at 2.2 Å^2 (1.26) and 1.8–2.3 Å^2 (1.16–1.21), respectively. At the Ca4 site, the B-factor of the Ca4 ion was larger than that of the interacting residues (Figure 5E) at 7 Å^2 (1.20) and 1.9–3.4 Å^2 (1.15–1.31), respectively.
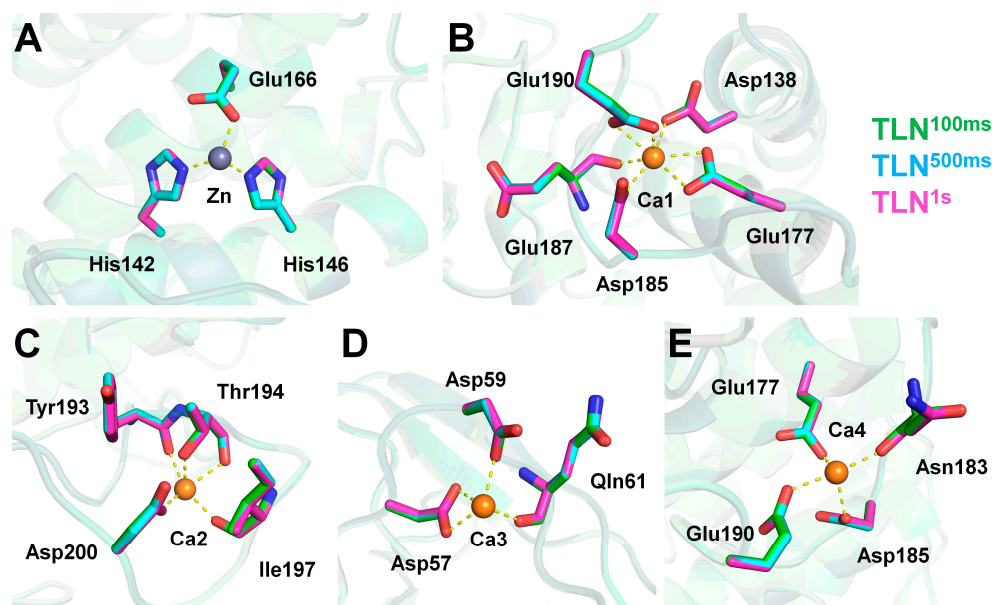
Figure 4. Superimposition of metal-binding site of TLNs at (**A**) Zn, (**B**) Ca1, (**C**) Ca2, (**D**) Ca3, and (**E**) Ca4 sites from TLN^{100ms} (green), TLN^{500ms} (cyan), and TLN^{1s} (pink).
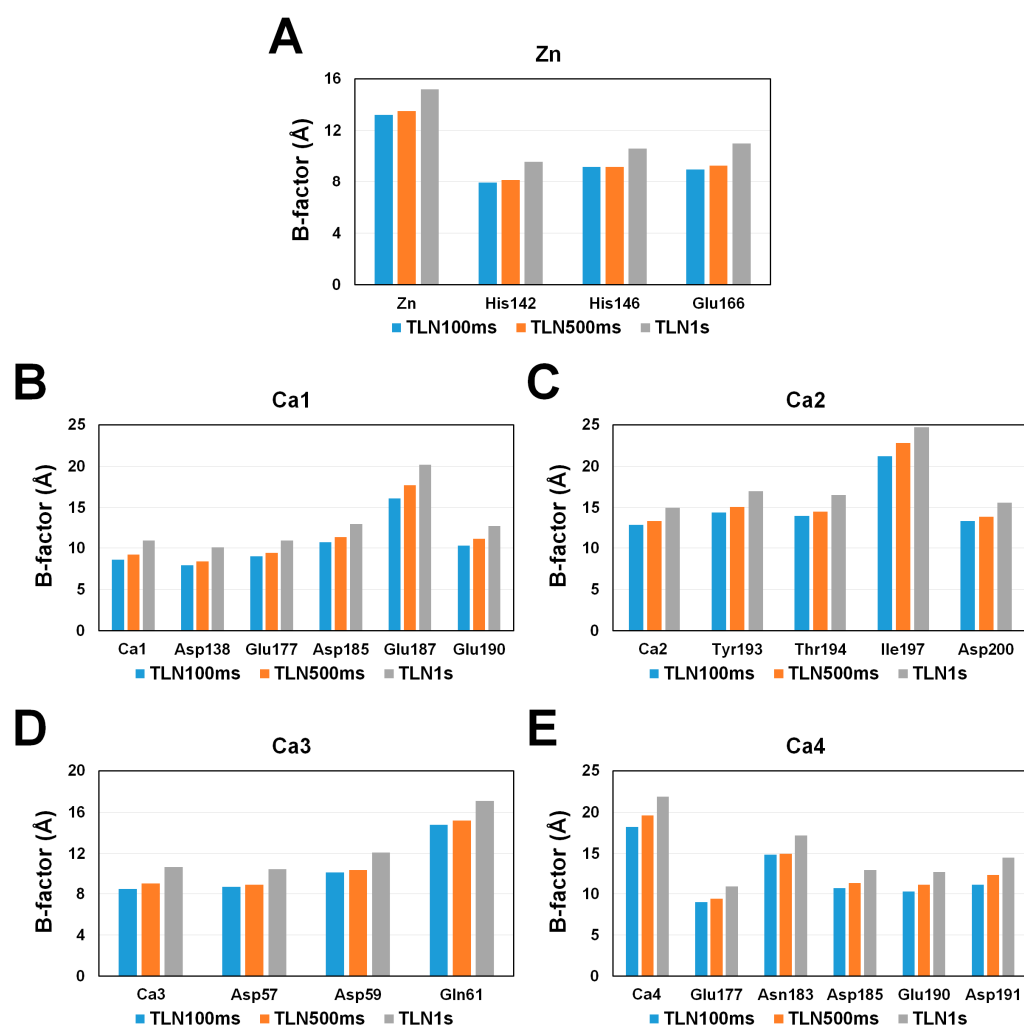

Figure 5. B-factor analysis of metal ions and their interacting residues of TLNs at (**A**) Zn, (**B**) Ca1, (**C**) Ca2, (**D**) Ca3, and (**E**) Ca4 sites from TLN^{100ms} (green), TLN^{500ms} (cyan), and TLN^{1s} (pink).

Upon increasing X-ray exposure, the increase in the absolute B-factor of the metal ion at the Ca4 site was greater than that of the interacting amino acids, whereas the absolute increase in the B-factors of metal ions at other Zn, Ca1, Ca2, and Ca3 sites was not always larger than that of their interacting amino acids. The normalized B-factor of the metal ion at the Ca3 site was larger than that of the interacting amino acids upon increasing X-ray exposure, whereas the normalized B-factor of metal ions at other Zn, Ca1, Ca2, and Ca4 sites was not always larger than that of their interacting amino acids. Consequently, the B-factors of metal ions and their interacting amino acids increased with increasing X-ray dose, but the metal ions did not exhibit a significantly larger change in B-factor compared with their interacting amino acids.

4. Discussion

In this study, the effects of X-ray doses on radiation damage in TLN crystals were investigated to enhance our understanding of radiation damage to metal ions within proteins. As observed during data collection, the quality of statistical values such as I/sigma(I), R_{merge}, R_{meas}, and CC1/2 in TLN crystals deteriorated with increasing X-ray dose. Moreover, the structural analysis revealed an increase in B-factor values for metal ions with higher X-ray doses. However, unlike X-ray dose-dependent radiation damage, no significant changes were produced in the interaction distances between metal ions and interacting residues. This result indicates that despite radiation damage affecting the data collection and refinement statistics, as well as the B-factors, the interaction distances between metal ions and their interacting residues may remain relatively unaffected. Thus, although high-Z atoms are known to be sensitive to radiation damage, metal ions coordinated within the TLN protein may be less sensitive to radiation damage. Meanwhile, the B-factors for both proteins and metal ions increased as the X-ray dose increased. This suggests that the B-factor may become inaccurate because of radiation damage as the X-ray dose increases. Therefore, for data collection strategies, the X-ray dose should be reduced to minimize the increase in the B-factor caused by radiation damage.

In a similar previous study using larger thaumatin crystals exposed to microfocusing X-rays for 100 ms and 1 s per degree of rotation over 180° during data collection, specific radiation damage such as disulfide bond breaking was observed [52]. However, in this study, despite exposing the TLN crystals to a larger X-ray dose over 360° of rotation during data collection, no significant specific radiation damage was observed apart from an increase in B-factors. The difference in radiation damage may be due to the specific sensitivity of metal ions compared to that of disulfide bonds [53,54]. For example, the reduction of the metal center by X-ray irradiation can depend on the redox potential of the metal ions [39]. Redox-sensitive iron, copper, and disulfide bonds in proteins may be easily damaged by X-ray irradiation [55–58]. Meanwhile, Zn and Ca are known to be redox-insensitive [59,60], making it difficult to observe significant radiation damage caused by X-ray irradiation on electron density maps. Moreover, the observed specific radiation damage may vary depending on the properties of the crystal sample, such as crystal size and solvent content.

Despite observing radiation damage in this study, the absence of severe consequences, such as diffraction resolution reduction and extremely high B-factors, could be attributed to the protein and crystal properties. Additionally, the larger size of the crystal used in this experiment, compared to the microfocusing beam, may make it relatively less sensitive to radiation damage. For example, if the crystal sample is smaller than or equal to the X-ray beam, the entire crystal volume is continuously exposed to the X-ray, producing radiation damage throughout the sample. Conversely, if the crystal sample is larger than the X-ray beam, only the center aligned with the X-ray is continuously exposed, leading to localized radiation damage accumulation. For example, exposing cuboid-shaped insulin crystals of 10, 20, 50, 100, 200, and 300 μm in size to an X-ray beam (3.5 × 8.5 μm) with a photon flux of 1×10^{12} photons/s showed that the volumes of X-rays exposed in the crystals were 100%, 100%, 48%, 26%, 13.0%, and 8.7%, respectively. The average dose in these exposed

regions for 10, 20, 50, 100, 200, and 300 µm crystals was approximately 164.14, 51.40, 17.31, 7.92, 3.89, and 2.54 MGy, respectively. Consequently, when using microfocused beams with single-point data collection, larger crystal sizes result in lower average radiation damage. This indicates that larger crystal sizes can reduce average radiation damage and can be a strategic consideration for data collection using microfocusing beamlines. To systematically analyze radiation damage to metal ions in TLN in more detail, future studies could increase the X-ray dose or use smaller crystal samples for an improved understanding of radiation damage to metal ions in these proteins.

This study investigated radiation damage to metal ions in TLN crystals larger than the microfocusing beam. An increase in the B-factors at metal ion sites was observed with increasing X-ray dose, while the interaction distances between metal ions and coordinating residues remained unaffected. These findings not only enhance our understanding of adiation damage to metal ions, but also provide valuable insights for data collection strategies.

Data Availability Statement: The coordinates and structure-factor amplitudes for both structures have been deposited in the PDB under the accession codes 8ZM4 (TLN^{100ms}), 8ZM5 (TLN^{500ms}), and 8ZM6 (TLN^{1s}).

References

1. Smyth, M.S.; Martin, J.H. X-ray crystallography. *Mol. Pathol.* **2000**, *53*, 8–14. [CrossRef] [PubMed]
2. Su, X.D.; Zhang, H.; Terwilliger, T.C.; Liljas, A.; Xiao, J.; Dong, Y. Protein Crystallography from the Perspective of Technology Developments. *Crystallogr. Rev.* **2015**, *21*, 122–153. [CrossRef] [PubMed]
3. Maveyraud, L.; Mourey, L. Protein X-ray Crystallography and Drug Discovery. *Molecules* **2020**, *25*, 1030. [CrossRef] [PubMed]
4. Kim, I.J.; Kim, S.R.; Bornscheuer, U.T.; Nam, K.H. Engineering of GH11 Xylanases for Optimal pH Shifting for Industrial Applications. *Catalysts* **2023**, *13*, 1405. [CrossRef]
5. Aitipamula, S.; Vangala, V.R. X-ray Crystallography and its Role in Understanding the Physicochemical Properties of Pharmaceutical Cocrystals. *J. Indian Inst. Sci.* **2017**, *97*, 227–243. [CrossRef]
6. Batool, M.; Ahmad, B.; Choi, S. A Structure-Based Drug Discovery Paradigm. *Int. J. Mol. Sci.* **2019**, *20*, 2783. [CrossRef]
7. Anderson, A.C. The Process of Structure-Based Drug Design. *Biol. Chem.* **2003**, *10*, 787–797. [CrossRef]
8. Xu, Y.; Nam, K.H. Xylitol binding to the M1 site of glucose isomerase induces a conformational change in the substrate binding channel. *Biochem. Biophys. Res. Commun.* **2023**, *682*, 21–26. [CrossRef]
9. Jelsch, C.; Teeter, M.M.; Lamzin, V.; Pichon-Pesme, V.; Blessing, R.H.; Lecomte, C. Accurate protein crystallography at ultra-high resolution: Valence electron distribution in crambin. *Proc. Natl. Acad. Sci. USA* **2000**, *97*, 3171–3176. [CrossRef]
10. Laulumaa, S.; Kursula, P. Sub-Atomic Resolution Crystal Structures Reveal Conserved Geometric Outliers at Functional Sites. *Molecules* **2019**, *24*, 3044. [CrossRef]
11. Tan, L.; Tian, S.; Liu, X.; Zhang, W.; Wu, X.; Gong, Y. Emittance and energy spread compensation in future synchrotron light sources. *Nucl. Instrum. Methods Phys. Res. A* **2023**, *1052*, 168278. [CrossRef]
12. Kim, Y.; Cho, B.G.; Koo, T.Y. Design and simulation of a mirror-mitigated thermal load on Korea-4GSR hard X-ray undulator beamline optics. *J. Korean Phys. Soc.* **2022**, *81*, 273–277. [CrossRef]
13. Cho, B.-G.; Kim, Y.; Shin, S.; Koo, T.-Y. Comparative study of hard X-ray undulator beamline performance in the Korean 4GSR and the PLS-II. *J. Korean Phys. Soc.* **2021**, *78*, 467–475. [CrossRef]
14. Schroer, C.G.; Falkenberg, G. Hard X-ray nanofocusing at low-emittance synchrotron radiation sources. *J. Synchrotron Radiat.* **2014**, *21*, 996–1005. [CrossRef] [PubMed]

15. Kim, J.; Kim, H.-Y.; Park, J.; Kim, S.; Kim, S.; Rah, S.; Lim, J.; Nam, K.H. Focusing X-ray free-electron laser pulses using Kirkpatrick–Baez mirrors at the NCI hutch of the PAL-XFEL. *J. Synchrotron Radiat.* **2018**, *25*, 289–292. [CrossRef]

16. Gu, D.H.; Eo, C.; Hwangbo, S.A.; Ha, S.C.; Kim, J.H.; Kim, H.; Lee, C.S.; Seo, I.D.; Yun, Y.D.; Lee, W.; et al. BL-11C Micro-MX: A high-flux microfocus macromolecular-crystallography beamline for micrometre-sized protein crystals at Pohang Light Source II. *J. Synchrotron Radiat.* **2021**, *28*, 1210–1215. [CrossRef]

17. Kim, J.; Nam, K.H. X-ray-Induced Heating in the Vicinity of the X-ray Interaction Point. *Appl. Sci.* **2023**, *13*, 717. [CrossRef]

18. Shelley, K.L.; Garman, E.F. Quantifying and comparing radiation damage in the Protein Data Bank. *Nat. Commun.* **2022**, *13*, 1314. [CrossRef]

19. Gebicki, J.M.; Nauser, T. Initiation and Prevention of Biological Damage by Radiation-Generated Protein Radicals. *Int. J. Mol. Sci.* **2021**, *23*, 396. [CrossRef]

20. Sliz, P.; Harrison, S.C.; Rosenbaum, G. How does Radiation Damage in Protein Crystals Depend on X-Ray Dose? *Structure* **2003**, *11*, 13–19. [CrossRef]

21. Ravelli, R.B.G.; McSweeney, S.M. The 'fingerprint' that X-rays can leave on structures. *Structure* **2000**, *8*, 315–328. [CrossRef] [PubMed]

22. Murray, J.; Garman, E. Investigation of possible free-radical scavengers and metrics for radiation damage in protein cryocrystallography. *J. Synchrotron Radiat.* **2002**, *9*, 347–354. [CrossRef] [PubMed]

23. Carugo, O.; Carugo, K.D. When X-rays modify the protein structure: Radiation damage at work. *Trends Biochem. Sci.* **2005**, *30*, 213–219. [CrossRef] [PubMed]

24. Weiss, M.S.; Panjikar, S.; Mueller-Dieckmann, C.; Tucker, P.A. On the influence of the incident photon energy on the radiation damage in crystalline biological samples. *J. Synchrotron Radiat.* **2005**, *12*, 304–309. [CrossRef] [PubMed]

25. Corbett, M.C.; Latimer, M.J.; Poulos, T.L.; Sevrioukova, I.F.; Hodgson, K.O.; Hedman, B. Photoreduction of the active site of the metalloprotein putidaredoxin by synchrotron radiation. *Acta Crystallogr. Sect. D Biol. Crystallogr.* **2007**, *63*, 951–960. [CrossRef]

26. Garman, E.F. Radiation damage in macromolecular crystallography: What is it and why should we care? *Acta Crystallogr. Sect. D Biol. Crystallogr.* **2010**, *66*, 339–351. [CrossRef]

27. Burmeister, W.P. Structural changes in a cryo-cooled protein crystal owing to radiation damage. *Acta Crystallogr. Sect. D Biol. Crystallogr.* **2000**, *56*, 328–341. [CrossRef]

28. Nam, K.H. Radiation Damage on Selenomethionine-Substituted Single-Domain Substrate-Binding Protein. *Crystals* **2023**, *13*, 1620. [CrossRef]

29. McCoy, A.J.; Read, R.J. Experimental phasing: Best practice and pitfalls. *Acta Crystallogr. Sect. D Biol. Crystallogr.* **2010**, *66*, 458–469. [CrossRef]

30. Schmidt, M.; Šrajer, V.; Purwar, N.; Tripathi, S. The kinetic dose limit in room-temperature time-resolved macromolecular crystallography. *J. Synchrotron Radiat.* **2012**, *19*, 264–273. [CrossRef]

31. Matsui, Y.; Sakai, K.; Murakami, M.; Shiro, Y.; Adachi, S.-I.; Okumura, H.; Kouyama, T. Specific Damage Induced by X-ray Radiation and Structural Changes in the Primary Photoreaction of Bacteriorhodopsin. *J. Mol. Biol.* **2002**, *324*, 469–481. [CrossRef] [PubMed]

32. Taberman, H. Radiation Damage in Macromolecular Crystallography—An Experimentalist's View. *Crystals* **2018**, *8*, 157. [CrossRef]

33. Harding, M.M.; Nowicki, M.W.; Walkinshaw, M.D. Metals in protein structures: A review of their principal features. *Crystallogr. Rev.* **2010**, *16*, 247–302. [CrossRef]

34. Harding, M.M. The architecture of metal coordination groups in proteins. *Acta Crystallogr. Sect. D Biol. Crystallogr.* **2004**, *60*, 849–859. [CrossRef] [PubMed]

35. Zheng, H.; Chruszcz, M.; Lasota, P.; Lebioda, L.; Minor, W. Data mining of metal ion environments present in protein structures. *J. Inorg. Biochem.* **2008**, *102*, 1765–1776. [CrossRef] [PubMed]

36. Dokmanić, I.; Šikić, M.; Tomić, S. Metals in proteins: Correlation between the metal-ion type, coordination number and the amino-acid residues involved in the coordination. *Acta Crystallogr. Sect. D Biol. Crystallogr.* **2008**, *64*, 257–263. [CrossRef]

37. Neufeld, M.J.; Lutzke, A.; Pratx, G.; Sun, C. High-Z Metal–Organic Frameworks for X-ray Radiation-Based Cancer Theranostics. *Chem. Eur. J.* **2020**, *27*, 3229–3237. [CrossRef]

38. Yano, J.; Kern, J.; Irrgang, K.-D.; Latimer, M.J.; Bergmann, U.; Glatzel, P.; Pushkar, Y.; Biesiadka, J.; Loll, B.; Sauer, K.; et al. X-ray damage to the Mn4Ca complex in single crystals of photosystem II: A case study for metalloprotein crystallography. *Proc. Natl. Acad. Sci. USA* **2005**, *102*, 12047–12052. [CrossRef]

39. Pfanzagl, V.; Beale, J.H.; Michlits, H.; Schmidt, D.; Gabler, T.; Obinger, C.; Djinović-Carugo, K.; Hofbauer, S. X-ray–induced photoreduction of heme metal centers rapidly induces active-site perturbations in a protein-independent manner. *J. Biol. Chem.* **2020**, *295*, 13488–13501. [CrossRef]

40. Wuerges, J.; Lee, J.-W.; Yim, Y.-I.; Yim, H.-S.; Kang, S.-O.; Carugo, K.D. Crystal structure of nickel-containing superoxide dismutase reveals another type of active site. *Proc. Natl. Acad. Sci. USA* **2004**, *101*, 8569–8574. [CrossRef]

41. Bury, C.S.; Brooks-Bartlett, J.C.; Walsh, S.P.; Garman, E.F. Estimate your dose: RADDOSE-3D. *Protein Sci.* **2018**, *27*, 217–228. [CrossRef] [PubMed]

42. Otwinowski, Z.; Minor, W. Processing of X-ray diffraction data collected in oscillation mode. *Methods Enzymol.* **1997**, *276*, 307–326. [CrossRef]

43. Vagin, A.; Teplyakov, A. Molecular replacement with MOLREP. *Acta Crystallogr. Sect. D Biol. Crystallogr.* **2010**, *66*, 22–25. [CrossRef]

44. Agirre, J.; Atanasova, M.; Bagdonas, H.; Ballard, C.B.; Baslé, A.; Beilsten-Edmands, J.; Borges, R.J.; Brown, D.G.; Burgos-Mármol, J.J.; Berrisford, J.M.; et al. The CCP4 suite: Integrative software for macromolecular crystallography. *Acta Crystallogr. Sect. D Struct. Biol.* **2023**, *79*, 449–461. [CrossRef] [PubMed]

45. Nam, K.H. Structural analysis of metal chelation of the metalloproteinase thermolysin by 1,10-phenanthroline. *J. Inorg. Biochem.* **2021**, *215*, 111319. [CrossRef] [PubMed]

46. Emsley, P.; Cowtan, K. Coot: Model-building tools for molecular graphics. *Acta Crystallogr. Sect. D Biol. Crystallogr.* **2004**, *D60*, 2126–2132. [CrossRef]

47. Murshudov, G.N.; Skubak, P.; Lebedev, A.A.; Pannu, N.S.; Steiner, R.A.; Nicholls, R.A.; Winn, M.D.; Long, F.; Vagin, A.A. REFMAC5 for the refinement of macromolecular crystal structures. *Acta Crystallogr. Sect. D Biol. Crystallogr.* **2011**, *67*, 355–367. [CrossRef]

48. Williams, C.J.; Headd, J.J.; Moriarty, N.W.; Prisant, M.G.; Videau, L.L.; Deis, L.N.; Verma, V.; Keedy, D.A.; Hintze, B.J.; Chen, V.B.; et al. MolProbity: More and better reference data for improved all-atom structure validation. *Protein Sci.* **2018**, *27*, 293–315. [CrossRef]

49. Zheng, H.; Cooper, D.R.; Porebski, P.J.; Shabalin, I.G.; Handing, K.B.; Minor, W. CheckMyMetal: A macromolecular metal-binding validation tool. *Acta Crystallogr. Sect. D Struct. Biol.* **2017**, *73*, 223–233. [CrossRef]

50. Roche, R.S.; Voordouw, G. The structural and functional roles of metal ions in thermolysin. *CRC Crit. Rev. Biochem.* **1978**, *5*, 1–23. [CrossRef]

51. Park, J.; Park, S.; Kim, J.; Park, G.; Cho, Y.; Nam, K.H. Polyacrylamide injection matrix for serial femtosecond crystallography. *Sci. Rep.* **2019**, *9*, 2525. [CrossRef] [PubMed]

52. Nam, K.H. Radiation Damage on Thaumatin: A Case Study of Crystals That Are Larger Than the Microfocusing X-ray Beam. *Appl. Sci.* **2023**, *13*, 1876. [CrossRef]

53. Wherland, S.; Pecht, I. Radiation chemists look at damage in redox proteins induced by X-rays. *Proteins* **2018**, *86*, 817–826. [CrossRef]

54. Nass, K. Radiation damage in protein crystallography at X-ray free-electron lasers. *Acta Crystallogr. Sect. D Struct. Biol.* **2019**, *75*, 211–218. [CrossRef]

55. Koppenol, W.H.; Hider, R.H. Iron and redox cycling. Do's and don'ts. *Free Radic. Biol. Med.* **2019**, *133*, 3–10. [CrossRef]

56. Leclercq, B.; Kabbour, H.; Arevalo-Lopez, A.M.; Daviero-Minaud, S.; Minaud, C.; David, R.; Mentré, O. Synthesis, structure and magnetic behavior of iron arsenites with hierarchical magnetic units. *Inorg. Chem. Front.* **2020**, *7*, 3987–3999. [CrossRef]

57. Hu, N.; Li, X.-Y.; Liu, S.-M.; Wang, Z.; He, X.-K.; Hou, Y.-X.; Wang, Y.-X.; Deng, Z.; Chen, L.-H.; Su, B.-L. Enhanced stability of highly-dispersed copper catalyst supported by hierarchically porous carbon for long term selective hydrogenation. *Chin. J. Catal.* **2020**, *41*, 1081–1090. [CrossRef]

58. Bhattacharyya, R.; Dhar, J.; Ghosh Dastidar, S.; Chakrabarti, P.; Weiss, M.S. The susceptibility of disulfide bonds towards radiation damage may be explained by S...O interactions. *IUCrJ* **2020**, *7*, 825–834. [CrossRef]

59. Chevion, M.; Korbashi, P.; Katzhandler, J.; Saltman, P. Zinc—A Redox-Inactive Metal Provides a Novel Approach for Protection Against Metal-Mediated Free Radical Induced Injury: Study of Paraquat Toxicity in *E. coli*. In *Antioxidants in Therapy and Preventive Medicine*; Advances in Experimental Medicine and Biology; Springer: Berlin/Heidelberg, Germany, 1990; pp. 217–222. [CrossRef]

60. Saito, K.; Nakagawa, M.; Mandal, M.; Ishikita, H. Role of redox-inactive metals in controlling the redox potential of heterometallic manganese–oxido clusters. *Photosynth. Res.* **2021**, *148*, 153–159. [CrossRef]